

# Trends and seasonality of 2019–2023 global methane emissions inferred from a localized ensemble transform Kalman filter (CHEEREIO v1.3.1) applied to TROPOMI satellite observations

Drew C. Pendergrass<sup>1</sup>, Daniel J. Jacob<sup>1</sup>, Nicholas Balasus<sup>1</sup>, Lucas Estrada<sup>1</sup>, Daniel J. Varon<sup>1</sup>, James D. East<sup>1</sup>, Megan He<sup>1</sup>, Todd A. Mooring<sup>2</sup>, Elise Penn<sup>2</sup>, Hannah Nesser<sup>3</sup>, and John R. Worden<sup>3</sup>

<sup>1</sup> School of Engineering and Applied Sciences, Harvard University, Cambridge, MA, USA

<sup>2</sup> Department of Earth and Planetary Sciences, Harvard University, Cambridge, MA, USA

<sup>3</sup> Jet Propulsion Laboratory, California Institute of Technology, Pasadena, CA, USA

*Correspondence to:* Drew Pendergrass (pendergrass@g.harvard.edu)

**Abstract.** We use 2019-2023 TROPOMI satellite observations of atmospheric methane to quantify global emissions at monthly  $2^\circ \times 2.5^\circ$  resolution with a localized ensemble transform Kalman filter (LETKF) inversion, deriving monthly posterior estimates of emissions and year-to-year evolution. We evaluate the sensitivity of the inversion to the assumed wetland distribution by using two alternative wetland inventories (WetCHARTs and LPJ-wsl) as prior estimates. Our best posterior estimate of global emissions shows a surge from 560 Tg a<sup>-1</sup> in 2019 to 587-592 Tg a<sup>-1</sup> in 2020-2021 before declining to 572-570 Tg a<sup>-1</sup> in 2022-2023. Posterior emissions reproduce the observed 2019-2023 trends in methane concentrations at NOAA surface sites and from TROPOMI with minimal regional bias. Consistent with previous studies, we attribute the 2020-2021 methane surge to a 14 Tg a<sup>-1</sup> increase in emissions from sub-Saharan Africa but find that previous attribution of this surge to anthropogenic sources (livestock) reflects errors in the assumed wetland spatial distribution. Correlation with GRACE-FO inundation data suggests wetlands in South Sudan played a major role in the 2020-2021 surge but are poorly represented in wetland models. By contrast, boreal wetland emissions decreased over 2020-2023 consistent with drying measured by GRACE-FO. We find that the global seasonality of methane emissions is influenced by northern tropical wetlands and peaks in September, later than the July wetland model peak and consistent with GRACE-FO. We find no global seasonality in oil/gas emissions, but US fields show elevated cold season emissions that could reflect increased leakage.

**Plain language summary.** We use satellite observations of atmospheric methane, a potent greenhouse gas, to calculate emissions from both human and natural sources. We find that methane emissions surged in 2020 and 2021 before declining in 2022 and 2023. We attribute the surge in large part to emissions from eastern Africa, which experienced large methane-generating floods. We argue that previous work has attributed the methane surge to human-caused emissions (rather than wetlands) because of poor mapping in the tropics.

# 1 Introduction

35 Methane is a strong greenhouse gas, contributing 0.6 °C of warming from the pre-industrial baseline, with  
a relatively short lifetime of about 9 years due principally to oxidation by the hydroxyl (OH) radical in  
the troposphere (Prather et al., 2012; Naik et al., 2021). Methane is emitted by natural sources, mostly  
wetlands, and by anthropogenic sources including enteric fermentation and manure from livestock, oil  
and gas, coal mining, rice, landfills, and wastewater (Saunois et al., 2025). Decreasing methane emissions  
40 is an effective way to mitigate climate change in the near-term while also achieving air quality co-benefits  
from reduced tropospheric ozone (West et al., 2006; Nisbet et al., 2020). Bottom-up methane emission  
inventories link emissions to processes (IPCC, 2019), but inventory construction typically lags by several  
years behind real time and is subject to errors. Satellite observations of atmospheric methane can help  
improve and update inventories through inverse analyses using Bayesian optimization and can offer  
45 insights on recent and rapid changes (Jacob et al., 2016; Houweling et al., 2017; Jacob et al., 2022). Here  
we apply a Localized Ensemble Transform Kalman Filter (LETKF) to TROPospheric Monitoring  
Instrument (TROPOMI) satellite observations of atmospheric methane for 2018-2023 to quantify  
emissions on a monthly basis and attribute the causes of the methane increase.

Global methane concentrations increased at a rate of 6-10 ppb a<sup>-1</sup> prior to 2019, surging to 13-18  
50 ppb a<sup>-1</sup> in 2020-2022 before returning to 10 ppb a<sup>-1</sup> in 2023 (NOAA, 2024). The causes of the methane  
surge are uncertain and have been variably attributed to wetlands or a decrease in OH (Qu et al., 2022;  
Peng et al., 2022; Drinkwater et al., 2023; Qu et al., 2024). Earlier increases have been attributed to  
emissions increases from oil and gas, livestock, and wetlands, with changes in the <sup>13</sup>C-CH<sub>4</sub> isotopic  
abundance pointing towards a biogenic source (Hausmann et al., 2016; Zhang et al., 2021; Basu et al.,  
55 2022). Global daily observations from TROPOMI, launched in 2017 (Lorente et al., 2021), provide a  
unique dataset to attribute methane trends including seasonal information.

LETKF (Hunt et al., 2007) uses an ensemble of chemical transport model (CTM) simulations of  
methane concentrations over short successive assimilation time windows to relate emissions to  
atmospheric concentrations. This ensemble approximates the background error covariance matrix which  
60 represents the prior uncertainty in the system. The LETKF algorithm has been used previously to analyze  
methane emissions and their trends (Feng et al., 2017; Bisht et al., 2023; Zhu et al., 2022). It has  
advantages compared to other inverse methods reviewed by Brasseur and Jacob (2017) in being far less  
computationally expensive than analytical methods, not requiring a model adjoint like in 4D-Var  
methods, and not being restricted dimensionally like Markov chain Monte Carlo methods. The short  
65 assimilation time window reduces the effect of errors in model transport (Yu et al., 2021) or in the  
seasonality of the prior estimate (East et al., 2024).

Here we estimate global methane emissions at 2°×2.5° spatial resolution and monthly temporal  
resolution from May 2018 through December 2023. We use the CHEEREIO platform (Pendergrass et al.,  
2023) to apply LETKF to the TROPOMI data. CHEEREIO is a general user-friendly platform for LETKF  
70 data assimilation powered by the GEOS-Chem CTM. We use the results to analyze seasonal and 2019-  
2023 trends in methane emissions from different emission sectors.

## 2 Data assimilation system

We use methane observations from TROPOMI (section 2.1) to optimize global methane emissions at  $2^\circ \times 2.5^\circ$  resolution (section 2.2) with the LETKF algorithm (section 2.3) implemented through CHEEREIO (section 2.4). We apply a downscaling approach to attribute emissions to different sectors at a finer scale than the  $2^\circ \times 2.5^\circ$  resolution of the inversion (section 2.5).

### 2.1 Observations

TROPOMI detects solar backscatter in the  $2.3 \mu\text{m}$  methane absorption band with global daily coverage at  $5.5 \times 7 \text{ km}^2$  nadir pixel resolution ( $7 \times 7 \text{ km}^2$  before August 2019) and 13:30 local solar time. We use the operational retrieval of dry-column methane mixing ratios ( $X_{\text{CH}_4}$ ) from the Netherlands Institute for Space Research (SRON) (Lorente et al., 2023), corrected for bias with a machine-learning algorithm trained on collocated data from the more precise but much sparser GOSAT satellite instrument (Balasus et al., 2023; obtained from <https://registry.opendata.aws/blended-tropomi-gosat-methane>. Last accessed: 27 Feb 2025).

We filter out retrievals over coastlines (fractional-water pixels) and oceans (glint retrievals), which are subject to residual artifacts (Balasus et al. 2023). We also account for bias that could be introduced by extended periods of missing TROPOMI data, caused by outages of the Visible Infrared Imaging Radiometer Suite (VIIRS) which is used for cloud clearing (Borsdorff et al., 2024). Full TROPOMI data records are available for 2019-2021, but in 2022 no TROPOMI data is available between July 26 and August 23, and in 2023 retrievals begin to fail on July 26 and are fully missing between August 10 and August 30. This is the time of year when methane emission is at its peak (East et al., 2024), but LETKF would persist July emissions through the period of missing data and increase emissions suddenly when observations resume to correct a global bias. We account for this artifact in our estimates of interannual variability by scaling to the seasonality of 2021 emissions as follows:

$$x_{\text{yr}} = x_{2021} \cdot \frac{x_{\text{yr,valid}}}{x_{2021,\text{valid}}} \quad (1)$$

Here  $x_{\text{yr}}$  are annual posterior mean gridded emissions in  $\text{yr} \in \{2022, 2023\}$  after correction,  $x_{\text{yr,valid}}$  are annual posterior mean emissions excluding the period of missing data, and  $x_{2021,\text{valid}}$  are 2021 posterior emissions excluding the same period. When analyzing seasonality, we show either 2021 results or the 2019-2021 detrended mean seasonality to avoid bias due to missing observations.

### 2.2 GEOS-Chem, prior inventories, and prescribed methane sinks

GEOS-Chem is a three-dimensional CTM driven by assimilated meteorological data from the Modern-Era Retrospective analysis for Research and Applications, Version 2 (MERRA-2) of the NASA Global Modeling and Assimilation Office (GMAO). We use the GEOS-Chem methane simulation (Maasakkers et al., 2019) at  $2.0^\circ \times 2.5^\circ$  resolution. We initialize all ensemble members in 2018 with a 33-year GEOS-Chem simulation in which the methane field is controlled by time-varying gridded NOAA surface methane observations that are used as the simulation's lower boundary condition, thus properly initializing the stratosphere (Mooring et al., 2024).

Prior methane emissions are listed in **Table 1**. Prior estimates of emissions and loss include no trends over the study period (persisting 2019 values), so any trends in the posterior solution are due to observations. Anthropogenic emissions are assumed to be aseasonal, except for manure management and rice for which we apply seasonal scaling factors (Maasackers et al., 2016; Zhang et al., 2016a). For wetland emissions, we conduct parallel inversions with priors based on two alternative inventories: the nine-member high-performance subset of the WetCHARTs v1.3.1 inventory ensemble (Bloom et al., 2017; Ma et al., 2021), and the Lund–Potsdam–Jena Wald Schnee und Landschaft (LPJ-wsl) dynamic global vegetation model driven with assimilated meteorological data from MERRA-2 (Zhang et al., 2016b). The latter inventory, which we denote LPJ-MERRA2 in what follows, has been found previously to better match the observed global methane seasonality (East et al., 2024).

Table 1. Global methane sources ( $\text{Tg a}^{-1}$ ) for 2023

|                      | Prior estimate <sup>a</sup> | Posterior best estimate <sup>b</sup> |
|----------------------|-----------------------------|--------------------------------------|
| <b>Total</b>         | <b>529-574</b>              | <b>570</b>                           |
| <b>Anthropogenic</b> | <b>348</b>                  | <b>392</b>                           |
| Livestock            | 121*                        | 151                                  |
| Oil+Gas              | 50 <sup>†</sup>             | 60                                   |
| Coal                 | 34 <sup>†</sup>             | 26                                   |
| Rice                 | 39*                         | 36                                   |
| Waste                | 81*                         | 92                                   |
| Other                | 24*                         | 26                                   |
| <b>Natural</b>       | <b>181-226</b>              | <b>178</b>                           |
| Wetlands             | 148-193                     | 141                                  |
| Termites             | 12                          | 18                                   |
| Fires                | 19                          | 17                                   |
| Seeps                | 2                           | 2                                    |

<sup>a</sup>Prior emissions include no trends over 2018-2023. Ranges are defined by the two alternative prior estimates for wetlands, both at  $0.5^\circ \times 0.5^\circ$  monthly resolution for 2019: lower value is WetCHARTs v1.3.1 (Ma et al., 2021) higher value is LPJ-wsl driven by MERRA-2 meteorology (Zhang et al., 2016b). Prior non-fossil anthropogenic emissions are from the 2018 EDGARv6 inventory (Crippa et al., 2021), denoted \*, and fossil anthropogenic emissions are from the 2010-2019 Global Fuel Exploitation Inventory (GFEI) version 2.0 (Scarpelli et al., 2022), denoted <sup>†</sup>. All anthropogenic emissions are at  $0.1^\circ \times 0.1^\circ$  resolution and are overwritten by national gridded emissions for the contiguous US (Maasackers et al., 2016), Mexico (Scarpelli et al., 2020), and Canada (Scarpelli et al., 2021). Termite emissions ( $4^\circ \times 5^\circ$ ) are from Fung et al. (1991), fire emissions ( $0.25^\circ \times 0.25^\circ$ ) are from the 2019 Global Fire Emissions Database (GFED4) (van der Werf et al., 2017), and geological seeps ( $1^\circ \times 1^\circ$ ) are from Etiope et al. (2019) with global scaling to the annual total from Hmiel et al. (2020).

<sup>b</sup>Posterior emissions for 2023 from the LETKF with sources attributed via downscaling. Best estimate represents the mean of LPJ-MERRA2 and WetCHARTs posterior estimates both with and without methane concentrations in the state vector.

Loss of methane from oxidation by tropospheric OH is computed with global 3-D monthly mean OH fields from GEOS-Chem (Wecht et al., 2014), scaled so that methane’s lifetime due to loss to tropospheric OH matches the best estimate of 11.2 years derived from methyl chloroform observations (Prather et al., 2012; East et al., 2024). Additional minor methane sinks in GEOS-Chem include oxidation by tropospheric Cl (Wang et al., 2019), oxidation in the stratosphere (Mooring et al., 2024), and uptake by soils (Murguia-Flores et al., 2018), resulting in an overall methane lifetime of 9.4 years.

### 135 2.3 The LETKF algorithm

The LETKF algorithm optimizes a state vector of emissions and/or concentrations to minimize the Bayesian scalar cost function  $J(\mathbf{x})$  assuming Gaussian error probability density functions (pdfs; Hunt et al., 2007; Brasseur and Jacob, 2017):

$$J(\mathbf{x}) = (\mathbf{x} - \mathbf{x}^b)^T (\mathbf{P}^b)^{-1} (\mathbf{x} - \mathbf{x}^b) + \gamma (\mathbf{y} - H(\mathbf{x}))^T \mathbf{R}^{-1} (\mathbf{y} - H(\mathbf{x})) \quad (2)$$

Here  $\mathbf{x}$  is the state vector to be optimized,  $\mathbf{x}^b$  is the prior state vector,  $\mathbf{P}^b$  is the background (also called prior or forecast) error covariance matrix of the model prediction,  $\mathbf{y}$  is the TROPOMI observations,  $H(\cdot)$  is an observation operator that transforms the state vector  $\mathbf{x}$  from the state space to the observation space,  $\mathbf{R}$  is the observational error covariance matrix, and  $\gamma$  is a regularization constant to account for unresolved error correlation in the observations and is taken to be 0.1 following Qu et al., (2024).  $\mathbf{x}$  includes gridded  $2^\circ \times 2.5^\circ$  methane emission scaling factors over land excluding Antarctica (2737 state vector elements) to be applied to the prior estimates. In additional inversion ensemble runs, we simultaneously optimize methane concentrations along with emissions scaling factors (concatenating both in the state vector  $\mathbf{x}$ ) to avoid systematically attributing discrepancies between observations and background concentrations to errors in prior emissions. We do not optimize tropospheric OH (as the main methane sink) because of strong global error correlations that prevent constraining OH as a local variable in the LETKF localization routines (Penn et al., 2025).

In the LETKF,  $m$  ensemble members with different emissions are initialized at time  $t_0$  and the forward model (GEOS-Chem) is run in parallel for a user-specified time (termed the assimilation window) for each of these ensemble members. After the runs complete, we construct the state vectors  $\mathbf{x}_i^b$  for each ensemble member (indexed by  $i$ ). We localize the calculation within a 1500 km radius of the grid cell being optimized, considering only observations within that radius; this converts a single intractable large matrix problem into many embarrassingly parallel calculations for individual grid cells involving much smaller matrices. We weight observations by their distance from the target grid cell with the Gaspari-Cohn function, a piecewise polynomial resembling a bell curve with a value of 1 at the grid cell and 0 at 1500 km away (Gaspari and Cohn, 1999).

To optimize the methane emissions and/or concentrations of a given grid cell, we start from the background state vector  $\mathbf{x}_i^b$ , and form the background perturbation matrix  $\mathbf{X}^b$  from the  $m$  vector columns  $\mathbf{X}_i^b$ :

$$\mathbf{X}_i^b = \mathbf{x}_i^b - \overline{\mathbf{x}^b}; \quad \overline{\mathbf{x}^b} = \frac{1}{m} \sum_{i=1}^m \mathbf{x}_i^b \quad (3)$$

Here  $\mathbf{X}_i^b$  represents the  $i$ th column of the  $n \times m$  matrix  $\mathbf{X}^b$  where  $n$  is the length of the state vector; each column of  $\mathbf{X}^b$  consists of the state vector from an ensemble member minus the mean state vector. The model predictions made during the assimilation window must be compared to observations. Hence we construct background vectors of simulated observations  $\mathbf{y}_i^b$  and a corresponding simulated observation perturbation matrix  $\mathbf{Y}^b$  formed from the  $m$  vector columns  $\mathbf{Y}_i^b$ :

$$\mathbf{Y}_i^b = \mathbf{y}_i^b - \overline{\mathbf{y}^b}; \quad \mathbf{y}_i^b = H(\mathbf{x}_i^b); \quad \overline{\mathbf{y}^b} = \frac{1}{m} \sum_{i=1}^m \mathbf{y}_i^b \quad (4)$$

All simulated observations are timed to line up as close as possible with actual observations (in this case, within one hour).

170 The mean analysis (posterior) state vector in the original space is then given by (Hunt et al., 2007):

$$\bar{\mathbf{x}}^a = \bar{\mathbf{x}}^b + \gamma \mathbf{X}^b \bar{\mathbf{P}}^a (\mathbf{Y}^b)^T \mathbf{R}^{-1} (\mathbf{y} - \bar{\mathbf{y}}^b) \quad (5)$$

where  $\mathbf{y}$  is the vector of observations.  $\bar{\mathbf{P}}^a$  is an  $m \times m$  matrix computed as follows:

$$\bar{\mathbf{P}}^a = \left( ((m-1) \cdot \mathbf{I}) + \gamma (\mathbf{Y}^b)^T \mathbf{R}^{-1} \mathbf{Y}^b \right)^{-1} \quad (6)$$

where  $\mathbf{I}$  is the  $m \times m$  identity matrix. The analysis perturbation matrix is then given by

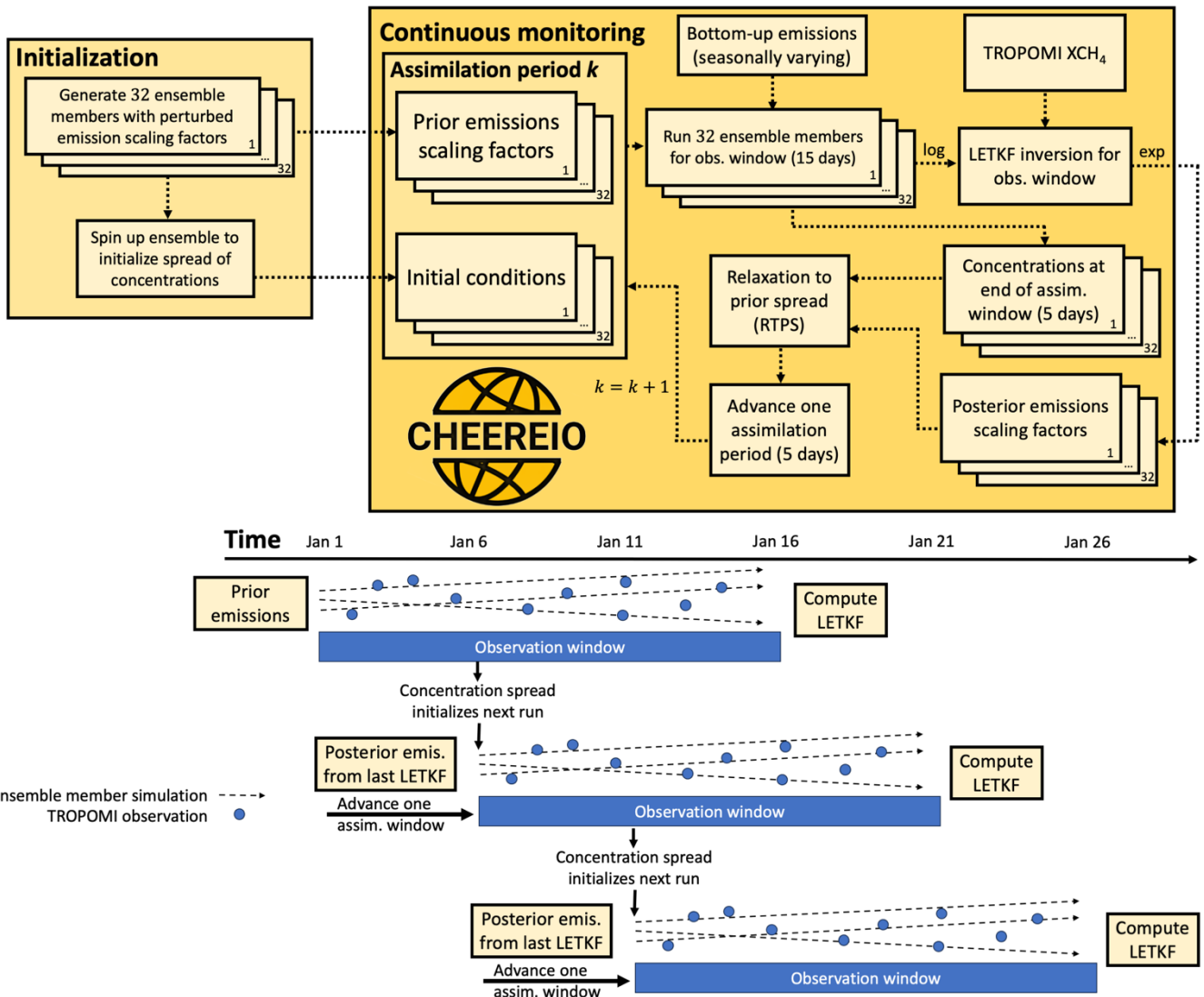
$$\mathbf{X}^a = \mathbf{X}^b \left( (m-1) \bar{\mathbf{P}}^a \right)^{\frac{1}{2}} \quad (7)$$

From here, the new ensemble state vectors can be constructed by adding  $\bar{\mathbf{x}}^a$  back to each column of  $\mathbf{X}^a$ . With the ensemble updated and errors characterized, the ensemble can be evolved using GEOS-Chem for the next assimilation window.

## 2.4 The CHEEREIO platform and LETKF settings

CHEEREIO is a lightweight wrapper of GEOS-Chem written in Python which allows users to conduct a range of LETKF applications by editing a single configuration file (Pendergrass et al., 2023). It takes advantage of GEOS-Chem's HEMCO emission module to update emissions without modifying the source code (Lin et al., 2021). Here we describe several new settings in the CHEEREIO v1.3.1 implementation of LETKF (<https://doi.org/10.5281/zenodo.11534085>), which we use in this work.

185 **Figure 1** shows the LETKF workflow as implemented in CHEEREIO v1.3.1. We apply the run-in-place (RIP) method to the LETKF assimilation window (Kalnay and Yang, 2010; Liu et al., 2019). With RIP, we calculate the LETKF assimilation update using a long period of observations (15 days, called the observation window), but then advance the assimilation window forward for a shorter period (5 days). RIP thus maintains linear growth in posterior perturbations and allows the system more time to assimilate information. Importantly, after advancing the assimilation window forward, we do not reinitialize the ensemble for new runs. Instead, the assimilated state of the previous observation window becomes the initial background state of the next assimilation window.



190

Figure 1: Flowchart of CHEEREIO v1.3.1 LETKF inversion procedure for assimilating TROPOMI methane data. We initialize a GEOS-Chem CTM simulations with randomized multiplicative perturbations to the prior estimates, applied to each of the 32 ensemble members. For assimilation period  $k$ , CHEEREIO runs GEOS-Chem for the observation window (15 days) for each ensemble member, then conducts the LETKF inversion by comparing the ensemble of GEOS-Chem values to the TROPOMI observations. over the observation window. Posterior emission scaling factors and concentrations are then inflated to reflect the prior spread using the RTPS procedure. The posterior emission estimates and inflated concentrations then become the prior estimate for the  $k+1$  assimilation period advancing by 5 days.

195

200

Because ensemble-based methods undersample the prior probability space, they suffer from shrinking dispersion between ensemble members which can lead to artificially small prior error estimation; an error inflation method is necessary to prevent ensemble collapse (Hunt et al., 2007). Following Bisht et al. (2023), we use the Relaxation to Prior Spread (RTPS) inflation method (Whitaker and Hamill, 2012). RTPS inflates the posterior ensemble standard deviation  $\sigma^a$  (defined as the standard

deviation of each state vector element) of such that it partially reflects the background ensemble standard deviation  $\sigma^b$ :

$$\mathbf{X}_{\text{infl}}^a = \left( \frac{\alpha_{\text{RTPS}} \sigma^b + (1 - \alpha_{\text{RTPS}}) \sigma^a}{\sigma^a} \right) \mathbf{X}^a \quad (8)$$

Here  $\alpha_{\text{RTPS}}$  is a parameter between 0 and 1 which represents the weighted contribution of the background standard deviation  $\sigma^b$  in inflating the analysis ensemble to obtain the final analysis perturbation matrix  $\mathbf{X}_{\text{infl}}^a$ . After sensitivity tests to mitigate underdispersed ensemble spread (shown by decreasing fidelity to observations over time), we take  $\alpha_{\text{RTPS}}$  to be 0.7, which is consistent with optimized values in Bisht et al. (2023). In the runs where only methane emissions are optimized, we additionally apply RTPS to 3D methane concentrations in the ensemble members even though we do not formally include concentrations in the state vector.

We perform our emissions estimates with an assumption of lognormal errors on the prior emission estimates, as is commonly done for analytical inversions (Maasakkers et al., 2019; Hancock et al., 2025) but to our knowledge has not previously been applied in the LETKF formalism. Lognormal errors better capture the upper tail of the methane emissions distribution than normal errors (Duren et al., 2019; Cusworth et al., 2022) and also prevents unphysical negative posterior emission estimates (Miller et al., 2014). However, a lognormal distribution across ensemble members violates the assumptions of the LETKF equations (Hunt et al., 2007). We solve this problem by sampling methane emissions scaling factors for each ensemble member according to a lognormal distribution centered on 1 (prior emission inventory) and run GEOS-Chem for each ensemble member with these scaling factors applied. When it is time for the LETKF calculation, we apply a logarithmic transform to the methane scaling factor distributions and thus obtain a normal distribution (centered on 0) for the construction of the background perturbation matrix  $\mathbf{X}^b$ . We perform the LETKF and once it is complete we apply an exponential to transform back to the original lognormal distribution, which is then used to evolve GEOS-Chem once more. These transformations are indicated as “log” and “exp” in **Figure 1**. The posterior solution is taken to be the median of the LETKF ensemble.

Before ingesting the TROPOMI observations into the LETKF, we aggregate the original observations into “super-observations” by averaging them onto the  $2.0^\circ \times 2.5^\circ$  GEOS-Chem grid (Eskes et al., 2003; Miyazaki et al., 2012; Pendergrass et al., 2023; Chen et al., 2023). To model the reduction in observational error variance due to averaging and obtain the super-observation error standard deviation  $\sigma_{\text{super}}$ , we follow a two-component error variance equation which separates contributions due to forward model transport error variance ( $\sigma_{\text{transport}}^2$ ) and error variance for a single retrieval ( $\sigma_i^2$ ):

$$\sigma_{\text{super}} = \sqrt{\left[ \left( \frac{1}{p} \sum_{i=1}^p \sigma_i \right) \cdot \left( \frac{1-c}{p} + c \right) \right]^2 + \sigma_{\text{transport}}^2} \quad (9)$$

Here  $p$  is the number of observations aggregated into a super-observation and  $c$  is the error correlation between the individual retrievals within a super-observation. The transport error is fully correlated. We take  $\sigma_i = 17$  ppb,  $\sigma_{\text{transport}} = 6.1$  ppb, and  $c = 0.28$  based on an empirical residual error method fit for TROPOMI methane (Chen et al., 2023; Pendergrass et al., 2023).

## 2.5 Sub-grid source attribution

Our inversion optimizes emissions on a  $2^{\circ}\times 2.5^{\circ}$  grid but the bottom-up inventories and TROPOMI data have much finer resolution ( $0.1^{\circ}\times 0.1^{\circ}$  for anthropogenic emissions,  $0.5^{\circ}\times 0.5^{\circ}$  for wetland emissions,  $7\times 7$  km<sup>2</sup> or  $5.5\times 7$  km<sup>2</sup> for TROPOMI observations at nadir). Here we exploit this high-resolution data with the source attribution approach of Yu et al. (2023), in which we conserve the overall posterior emissions in a  $2^{\circ}\times 2.5^{\circ}$  grid cell but adjust relative source contributions within it based on subgrid observational patterns. If TROPOMI observations are persistently elevated in a portion of the  $2^{\circ}\times 2.5^{\circ}$  grid cell associated with a particular sector, the Yu et al. (2023) methodology will attribute a larger fraction of the correction to that sector. We neglect subgrid prior error terms in Yu et al. (2023) to obtain a subgrid attribution based solely on the distribution of TROPOMI observations and prior sources. For wetlands we update the prior sources for individual years using LPJ-MERRA2.

Most grid cells are not affected significantly by this sub-grid source attribution approach, but we find substantial adjustments in a few regions including Sudd wetlands in South Sudan (where some livestock emissions are re-attributed to wetlands) and in Bangladesh (where some rice emissions are re-attributed to wetlands). Our global posterior wetlands emission increases by 10%, offset by decreases in the rice, livestock, and waste sectors.

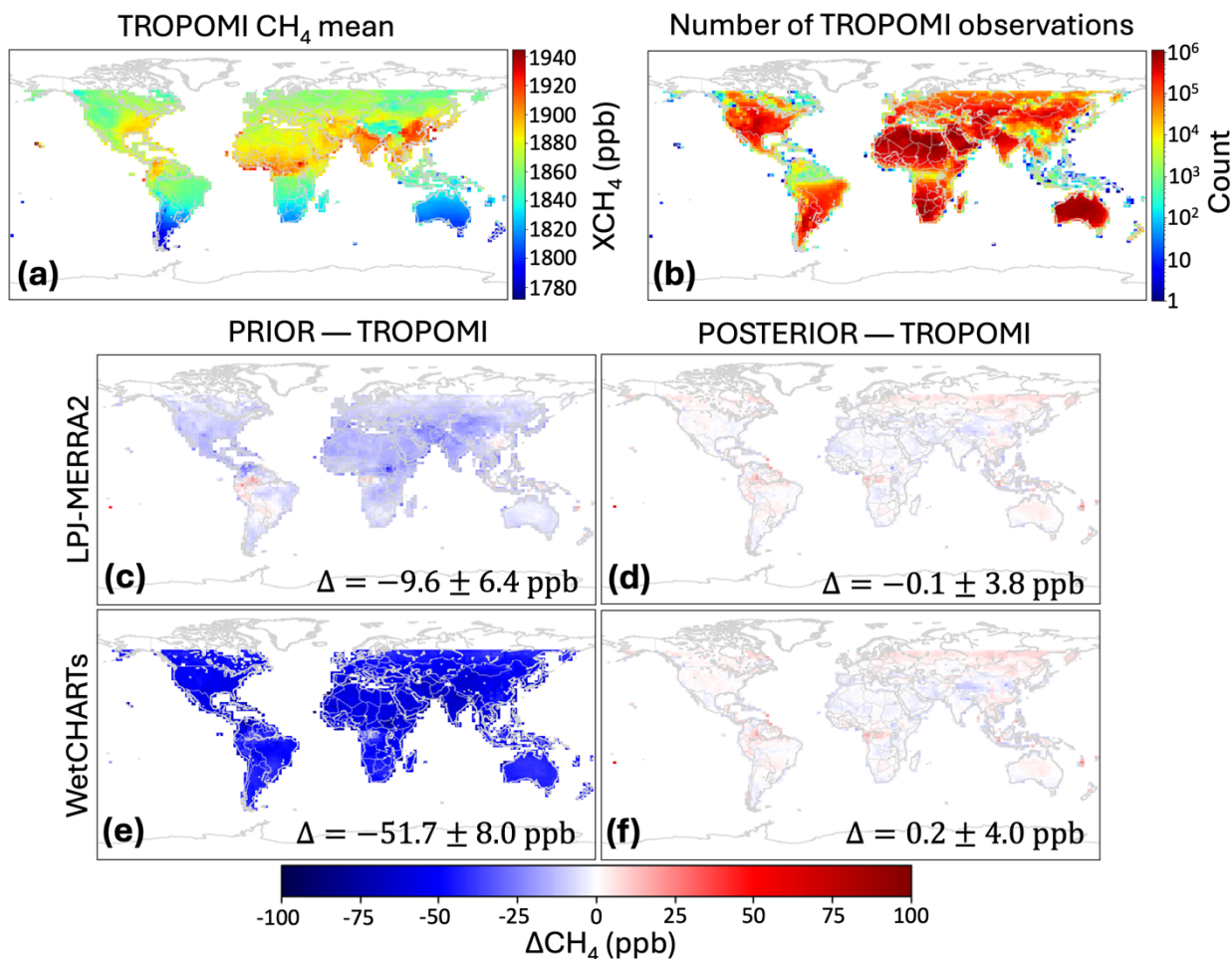
## 3 Results and discussion

Figure 2 shows TROPOMI methane dry column mixing ratios ( $X_{CH_4}$ ) for the study period, along with the corresponding GEOS-Chem model biases using prior and posterior emissions with either WetCHARTs or LPJ-MERRA2 as prior emissions for wetlands. The model with prior emissions has a low bias due to a methane budget imbalance. The posterior emissions eliminate this bias. Figure 3a shows the growth in global annual mean methane concentrations over the 2018-2023 study period. Trends in NOAA surface methane concentrations (NOAA, 2024) are consistent with TROPOMI trends as well as our posterior estimate. Figure 3b shows the posterior emissions from our four inversion ensemble members (driven with different wetlands and either optimizing concentrations and emissions or emissions alone), all predicting similar annual emissions. ( $577$  Tg a<sup>-1</sup> and  $567$  Tg a<sup>-1</sup> for WetCHARTs and LPJ-MERRA2 respectively in 2023). Seasonal CH<sub>4</sub> variability and trends in both hemispheres are also well-captured by the posterior (Figure 3cd).

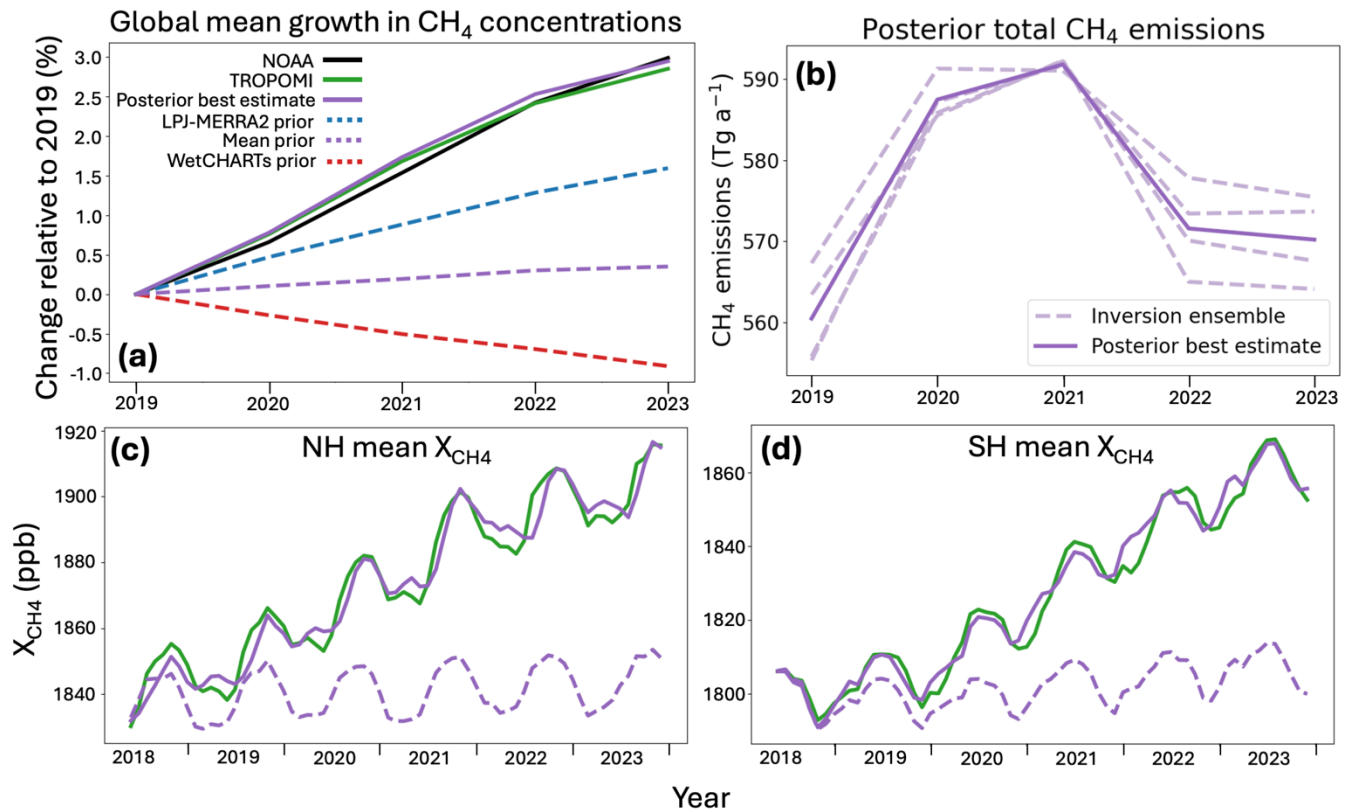
Posterior emissions for 2023 are summarized in Table 1. Our best posterior estimate of  $560$  Tg a<sup>-1</sup> for 2019 is within the  $556$ - $570$  Tg a<sup>-1</sup> range calculated for 2019 by Qu et al. (2021) and the  $553$ - $586$  Tg a<sup>-1</sup> range from top-down inversions for 2010-2019 reviewed in Saunio et al. (2025). In 2020 and 2021 we find that global methane emissions surged to  $587$  Tg a<sup>-1</sup> and  $592$  Tg a<sup>-1</sup> before declining to  $572$  Tg a<sup>-1</sup> in 2022 and  $570$  Tg a<sup>-1</sup> in 2023, consistent with the  $570$ - $590$  Tg a<sup>-1</sup> range for 2020-2022 reported in Qu et al. (2024) and the 2020 estimate of  $581$ - $627$  Tg a<sup>-1</sup> from Saunio et al. (2025). Our best estimate of fossil fuel emissions (oil, gas, and coal) for 2019 is  $88$  Tg a<sup>-1</sup>, intermediate between the  $80$  Tg a<sup>-1</sup> found in the 2019 analytical inversion of Qu et al. (2021) and the  $98$  Tg a<sup>-1</sup> estimate for 2018-19 from 4D-Var inversions done by Yu et al. (2023), but below the  $100$ - $124$  Tg a<sup>-1</sup> range for 2010-2019 in Saunio et al. (2025). Our  $265$  Tg a<sup>-1</sup> estimate for agricultural and waste emissions for 2019 is correspondingly above

275 the 213-242 Tg a<sup>-1</sup> range for 2010-2019 in Saunois et al. (2025), while our wetland posterior estimate of 150 Tg a<sup>-1</sup> falls within but at the low end of the 145-214 Tg a<sup>-1</sup> range from Saunois et al. (2025) and is lower than Qu et al. (2024).

### TROPOMI observations and model bias using prior and posterior emissions, 2018-2023



280 Figure 2: TROPOMI observations of methane dry column mixing ratios (XCH<sub>4</sub>) and comparison to GEOS-Chem simulations using either prior or posterior emissions. Values are averages for June 2018 through December 2023. ΔCH<sub>4</sub> denotes the difference between the simulation (with observation operators applied) and the observations. Global mean bias and spatial standard deviation are given inset. Results are shown for wetlands prior estimates from either LPJ-MERRA2 or WetCHARTs.



285

Figure 3: Global methane trends, 2018-2023. Panel (a) shows global annual mean observations from NOAA background surface sites ([https://gml.noaa.gov/ccgg/trends\\_ch4/](https://gml.noaa.gov/ccgg/trends_ch4/)), TROPOMI, and GEOS-Chem model simulations using prior emission estimates (including either WetCHARTs or LPJ-MERRA2 wetlands) and posterior emission estimates. The posterior represents the mean of the inversion ensemble. Panel (b) shows annual posterior methane emissions for the inversion ensemble, including either WetCHARTs or LPJ-MERRA2 wetlands and either with or without optimization of concentrations. Panels (c) and (d) show mean TROPOMI and GEOS-Chem results smoothed over monthly temporal resolution for the northern (c) and southern (d) hemispheres.

290

To understand the drivers of our posterior emissions trends, we disaggregate our results by region and sector (Figure 4). We find a negative trend in South American emissions which we attribute to a decline in wetland emissions; this is consistent in sign with other top-down work using GOSAT and surface observations finding decreases in 2020 and 2021 relative to 2019 in the Orinoco, Patanal, and Amazon Basin wetlands (Lin et al., 2024). We attribute the 2020 methane surge to a 14 Tg a<sup>-1</sup> increase in emissions from sub-Saharan Africa, as in previous studies (Qu et al., 2022; Feng et al., 2022), and we find that the elevated emissions persist into later years. Consistent with Qu et al. (2024), who find that wetland emissions are relatively constant over 2019-2022 and that anthropogenic emissions drive much of the 2020-2021 surge, we find that a surge in wetland emissions contributed to the 2020-2021 emissions peak but anthropogenic sectors including livestock and waste are more important (Figure 4b).

300

However, anthropogenic attribution of the African emission surge may be unreliable given uncertainty in tropical wetland prior inventories. Figure 5 compares our posterior emissions for the northern tropics and boreal latitudes with water storage from inundation as measured by the Gravity Recovery and Climate Experiment Follow-On (GRACE-FO) twin satellites, where the distance between the satellites is used to measure liquid water equivalent (LWE) thickness anomalies (cm) relative to a

305

time mean at monthly  $0.5^{\circ} \times 0.5^{\circ}$  resolution (Watkins et al., 2015; Wiese et al., 2016; Wiese et al., 2023). The northern tropics ( $0^{\circ}\text{N}$ - $30^{\circ}\text{N}$ ) explain much of the 2020-2021 surge and this corresponds closely with increases in water storage; consistently, the declining emission trend in boreal regions ( $50^{\circ}\text{N}$ - $90^{\circ}\text{N}$ ) corresponds with drying. Much of the northern tropics surge is associated with wetlands in South Sudan and southern Sudan, which account for 9% of prior emissions (mean of WetCHARTs and LPJ-MERRA2) in the  $0^{\circ}\text{N}$ - $30^{\circ}\text{N}$  band but for our posterior 2021-23 estimate they surge to almost a third; indeed, we find a  $7.5 \text{ Tg a}^{-1}$  increase from 2019 to 2021 in the region, accounting for a quarter of the global emissions increase in the same period. Our posterior solution predicts sharply increasing emissions after 2019 in the Sudd, Machar, and Lotilla wetlands in South Sudan, which experienced extensive flooding in 2020 and in following years and have been identified in previous work as globally significant drivers of the methane emissions trend (Pandey et al., 2021; Feng et al., 2022; Hardy et al., 2023). We attribute almost half of the  $7.5 \text{ Tg a}^{-1}$  increase in Sudan and South Sudan to anthropogenic sources (principally livestock) but this may reflect an underestimate of wetland area in the prior inventories.

Recent work indeed suggests that wetland extent in Africa may be underestimated due to sparse observational data (Dong et al., 2024). Wetlands in South Sudan especially are prone to underestimates from wetland models because emissions are driven by inflows from the White Nile and Sobat rivers rather than local precipitation (Pandey et al., 2021); the post-2020 period corresponds with record high water levels in Lake Victoria which feeds the White Nile (Dong et al., 2024). Neither the WetCHARTs nor the LPJ-MERRA2 inventories capture the surge in these wetlands. As a result, our inversion and the previous inversion of Qu et al. (2024) attribute the 2019-2021 methane surge to a 40% increase in livestock emissions in sub-Saharan Africa, This is inconsistent with Food and Agricultural Organization (FAO) cattle population data, which shows only an increase of 8% in 2023 relative to 2019 in the region (<https://www.fao.org/faostat>; last accessed: 2025-02-07). As Figure 6 shows, total emissions for the region including the increase after 2019 and seasonal emission peak are closely associated with GRACE-FO water storage data, while emissions attributed to wetlands in WetCHARTs or LPJ-MERRA2 do not reflect GRACE-FO trends.

We see from Figure 6 that inundation as measured by GRACE-FO is strongly correlated with the seasonality of methane emissions in sub-Saharan Africa. Figure 7 shows the global seasonal cycle of posterior methane emissions for 2021, avoiding missing TROPOMI observations in 2022-23. The global seasonality of methane emissions is mainly driven by the northern hemisphere. The seasonality of methane in the southern hemisphere (Figure 3) is largely driven by the OH sink (East et al., 2024). Unlike the prior estimates including WetCHARTs or LPJ-MERRA2 wetlands, which show a July-August peak in the northern hemisphere (Figure 7a), we find a sharp September peak driven by tropical emissions which strongly influences global seasonality (Figure 7b). Figure 7c shows that northern tropical emissions seasonality corresponds with the cycle of mean GRACE-FO water storage data. Livestock shows a seasonality in phase with wetlands, which as pointed out above could be due to misattribution in the tropics. Rice emissions in the northern hemisphere peak in July-September corresponding to the dominant growing season (Chen et al., 2025).

345

## CH<sub>4</sub> emissions change relative to 2019

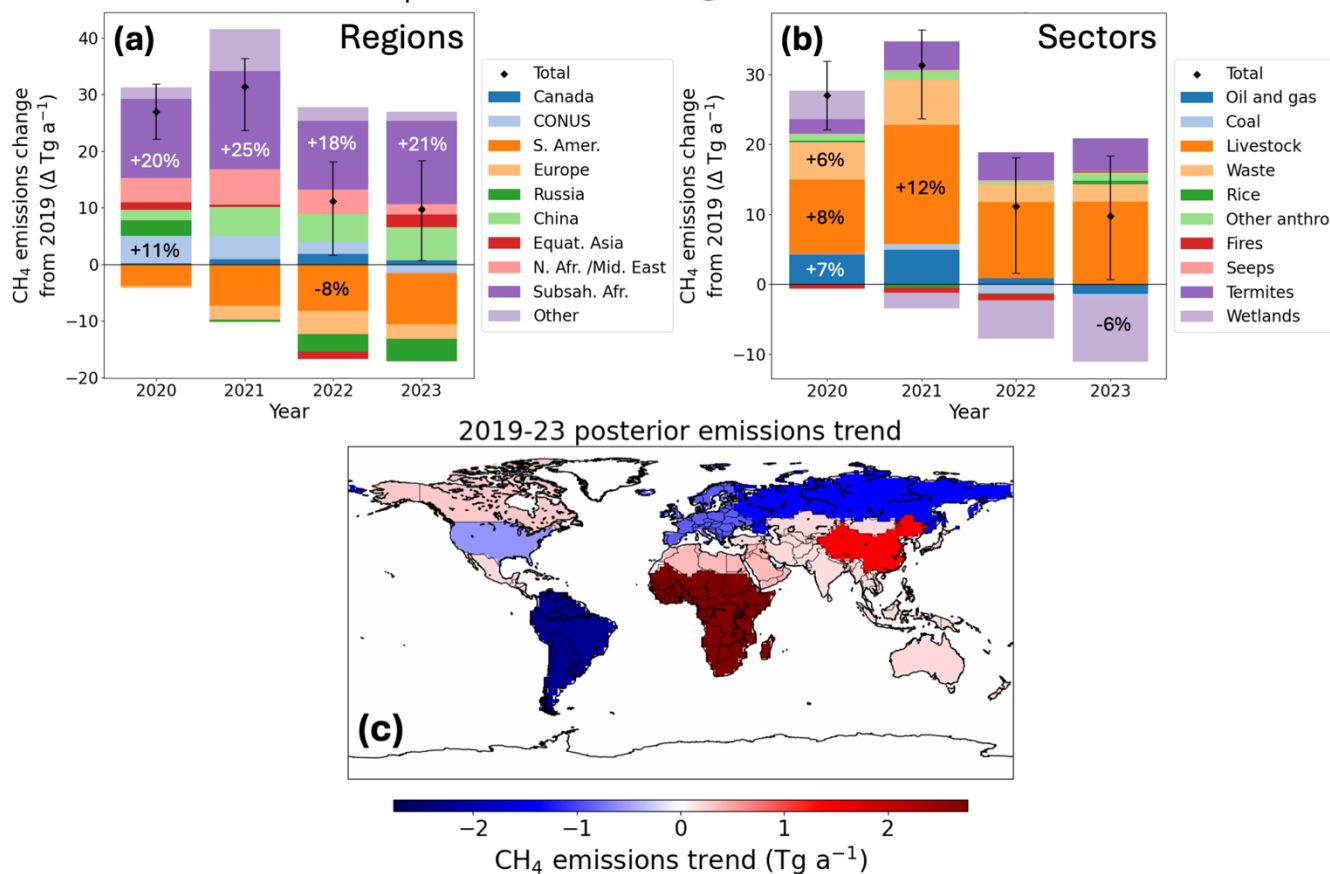


Figure 4: Annual emission trends for 2019-2023 disaggregated by region and sector. Panels (a) and (b) show posterior emission changes relative to 2019, disaggregated by region and sector respectively. Inset percentages show changes relative to 2019 values for selected regions/sectors. Error bars show range of inversion ensemble for the global emission trend. Panel (c) shows 2019-2023 trends in posterior emissions by region obtained from linear regression.

## Posterior emission and inundation annual trends

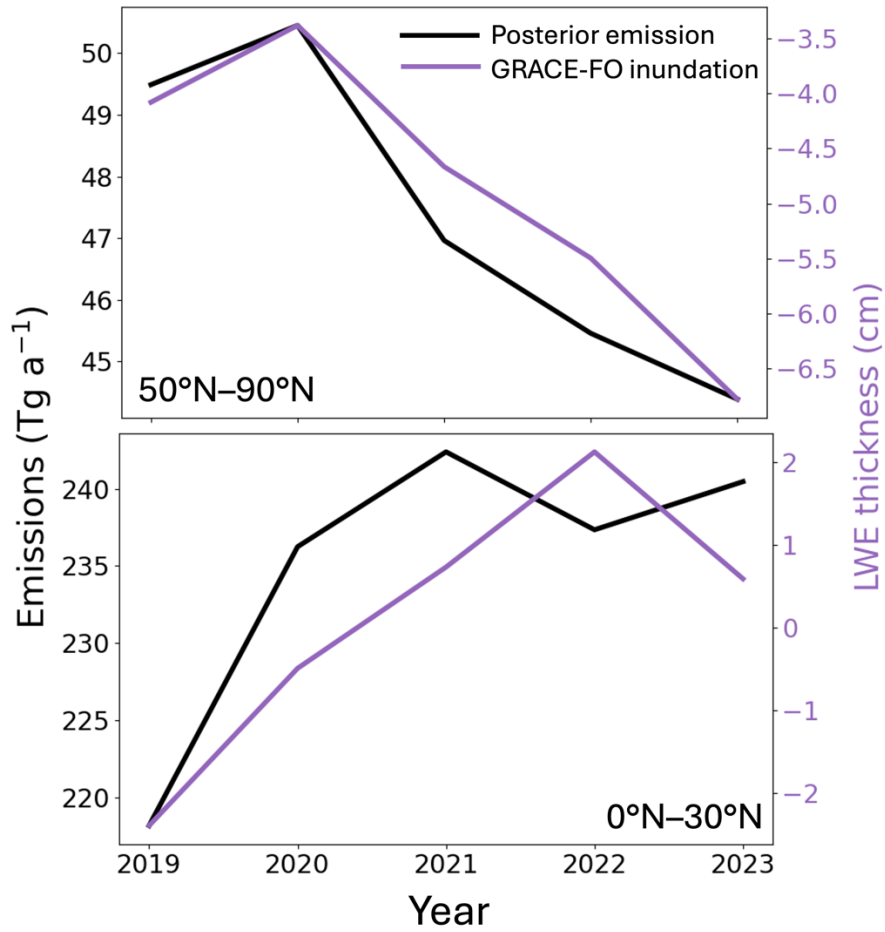


Figure 5: Inundation and posterior emission trends. Top panel compares total posterior emission north of 50°N with mean GRACE-FO liquid water equivalent (LWE) anomalies weighted by gridded total posterior emissions. Bottom panel is the same but for the northern tropics (0-30°N).

355

## Sub-Saharan emissions correlate with inundation

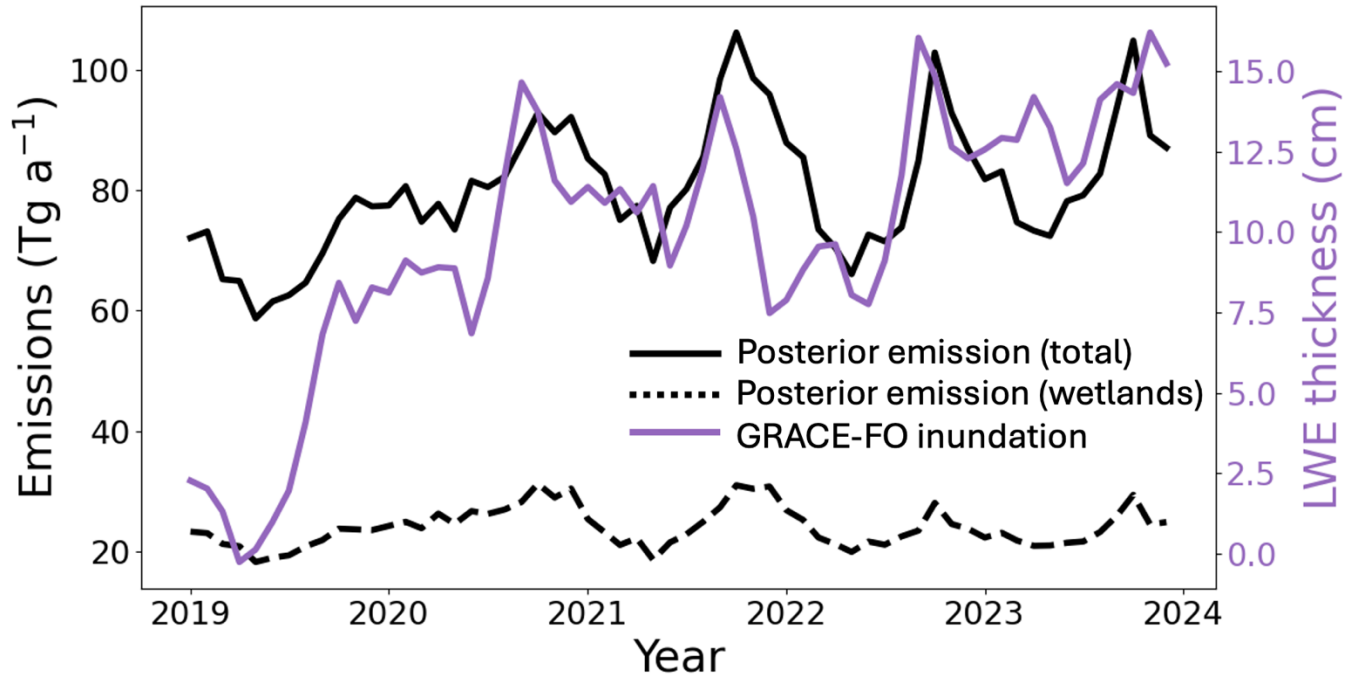
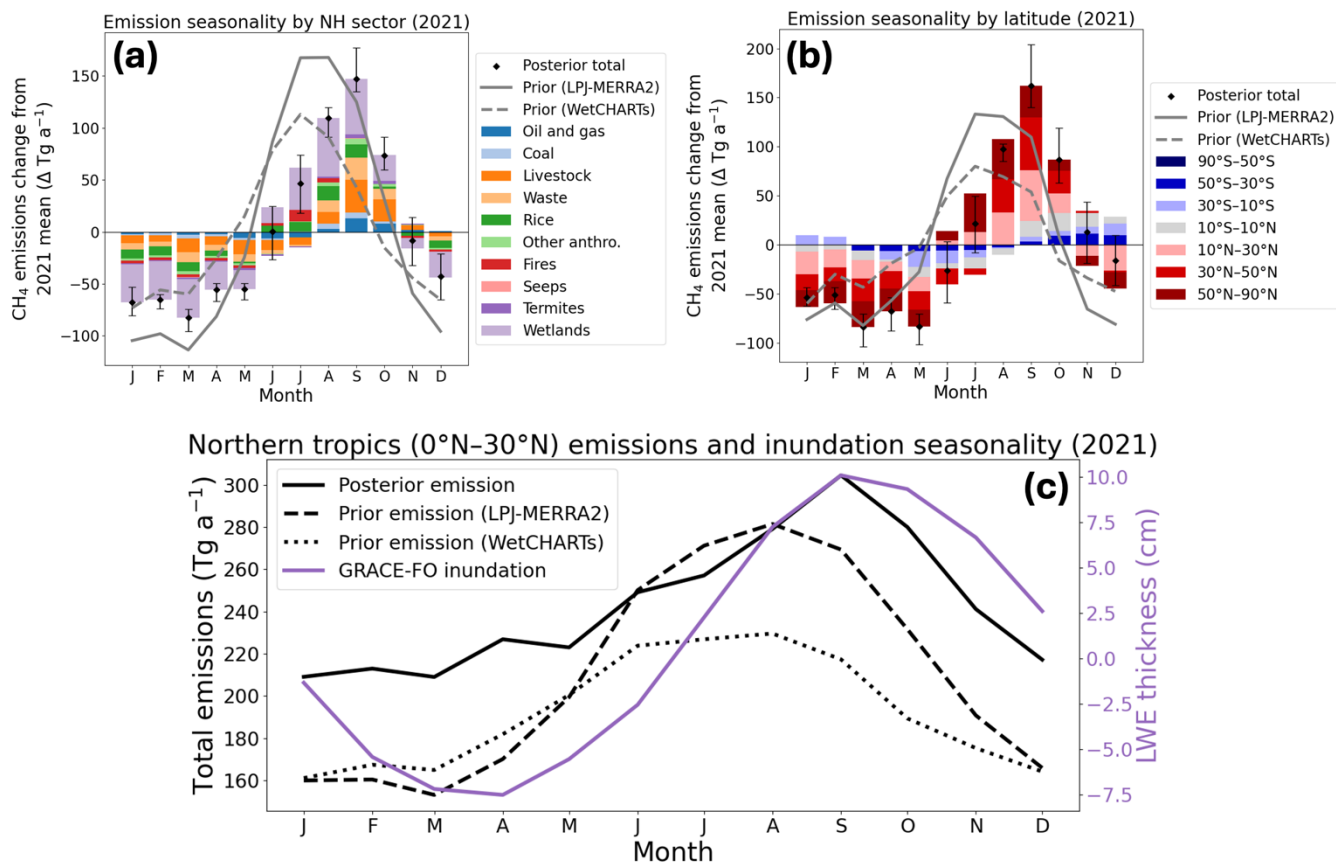


Figure 6: Inundation and posterior emissions trends in sub-Saharan Africa (region defined in Figure 4). The panel compares total and wetlands posterior emissions with mean GRACE-FO liquid water equivalent (LWE) anomalies. LWE is an average for the region, weighted by gridded total posterior emissions.



360

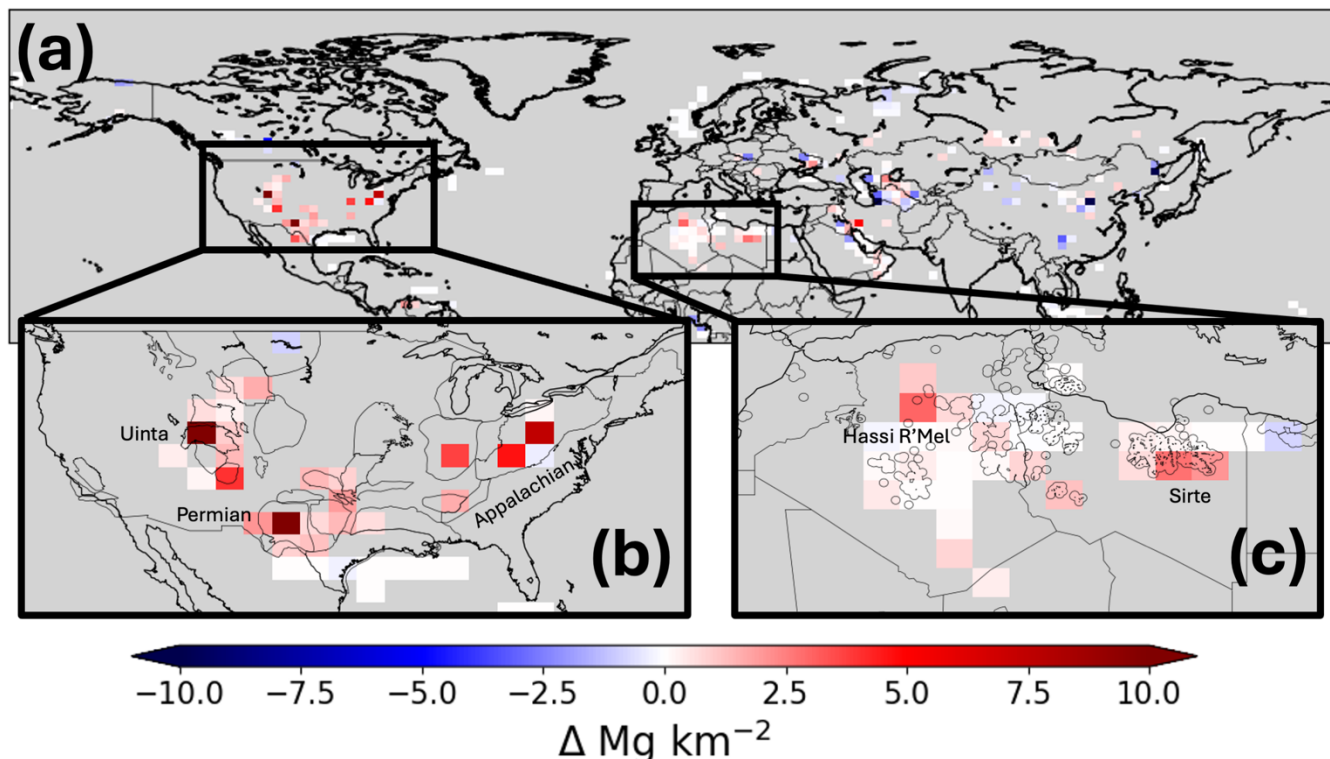
Figure 7. Posterior emission seasonality in 2021. Panel (a) shows northern hemisphere posterior emissions disaggregated by source sector, where the seasonal cycle is obtained by subtracting the 2021 mean. The prior seasonal cycle of total emissions is also shown in grey lines for both LPJ-MERRA2 and WetCHARTs wetlands. Panel (b) is as in panel (a) but global and disaggregated by latitude. Error bars show range of inversion ensemble. Panel (c) shows prior simulations driven by LPJ-MERRA2 and WetCHARTs wetlands with the posterior best estimate in the northern tropics (0°N-30°N), compared to mean GRACE-FO liquid water equivalent (LWE) anomalies in the region, weighted by gridded total posterior emissions.

365

Fossil fuel emissions are generally considered to be aseasonal but we observe seasonality in some production basins especially in the US. Figure 8 shows the difference in best-estimate posterior fossil fuel emissions in cold months minus warm months, with many areas showing elevated cold season emissions including several major US basins, Hassi R'Mel field (Algeria), Sirte basin (Libya), and West Karun basin (Iran). This phenomenon has been observed before in the Permian (Vanselow et al., 2024; Varon et al., in prep), but it is not seen worldwide and may suggest processes specific to the industry in the US and a few other regions. Possible causes include more frequent equipment failures in winter or emissions from poorly weatherized separator vessels, where more gas remains dissolved in liquid at cold temperatures and is vented later from liquids storage tanks (Varon et al., in prep).

375

## Cold minus warm season fossil emissions



380 Figure 8: Seasonality of oil and gas emissions for 2019-2021. Panel (a) shows northern hemisphere mean fossil fuel emissions in cold months (December through April) minus warm months (June through September) in grid cells where fossil fuels account for at least 50% of emissions. Inset (b) is as in (a) but for the contiguous US (CONUS), with major sedimentary basins overlaid; inset (c) is as in (a) but for Algeria and Libya, with oil and gas fields overlaid (Sabbatino et al., 2017).

## 4 Conclusions

385 We used the localized ensemble transform Kalman filter (LETKF) algorithm, deployed through the open-source CHEEREIO platform, to infer global methane emission trends and seasonalities by assimilation of TROPOMI satellite observations of atmospheric methane from May 2018 through December 2023 over 5-day time windows. Our goal was to understand the regions and source sectors driving the rapid increase of methane over that period and its seasonality. We used the blended TROPOMI product of Balasus et al. (2023) that corrects TROPOMI retrieval biases using machine learning applied to collocated observations from the GOSAT satellite instrument.

390 Our posterior emissions from the assimilation of TROPOMI data reproduce the observed 2019-2023 trends in methane concentrations at surface sites and from TROPOMI, with minimal regional bias. We estimate that emissions surged from 560 Tg a<sup>-1</sup> in 2019 to 587-592 Tg a<sup>-1</sup> in 2020-2021 before declining to 572-570 Tg a<sup>-1</sup> in 2022-2023, assuming no interannual change in tropospheric OH concentrations. Sub-Saharan Africa contributed 14 Tg a<sup>-1</sup> of the 27 Tg a<sup>-1</sup> global increase in 2020 and this contribution was sustained through 2023. Past attribution of this surge to anthropogenic sources may be  
395

due to errors in the spatial distribution of wetlands, as we find that the emission increases correspond closely with inundation as measured by the GRACE-FO satellite instrument. Wetlands in East Africa, particularly the Sudd, are instrumental in driving the methane trend but are poorly represented in current wetland emission models.

400 Methane emissions show a large seasonality and the high temporal resolution of our LETKF implementation allows us to probe its origin. We find that this seasonality is dominated by northern hemisphere wetland emissions and peaks in September, as opposed to July in wetland models. The September peak in the tropics closely follows inundation patterns. Oil and gas emissions show little seasonality globally but we find that production fields in the US have a distinct seasonal cycle of elevated  
405 emissions during the cold season.

Our CHEEREIO software toolkit is openly available (<https://doi.org/10.5281/zenodo.11534085>) as a general user-friendly implementation of LETKF for assimilating observations of atmospheric composition through the GEOS-Chem chemical transport model. In this work we introduced a novel approach to specify log-normal emissions errors within the LETKF framework, and this is released as  
410 part of CHEEREIO version 1.3.1.

## Data and code availability

The CHEEREIO source code is available at <https://github.com/drewpendergrass/CHEEREIO>; the version of CHEEREIO used in this paper (1.3.1) is archived at <https://doi.org/10.5281/zenodo.11534085> (Pendergrass et al., 2023). GEOS-Chem version 14.1.1 source code is archived at  
415 <https://doi.org/10.5281/zenodo.7696632>. The blended TROPOMI-GOSAT product is available at <https://registry.opendata.aws/blended-tropomi-gosat-methane> (Balasus et al., 2023) and NOAA surface data is available at ([https://gml.noaa.gov/ccgg/trends\\_ch4/](https://gml.noaa.gov/ccgg/trends_ch4/)). Wetland emissions from WetCHARTs v1.3.1 are available at <https://doi.org/10.3334/ORNLDAAAC/1915> (Ma et al., 2021) and from LPJ-wsl at <https://gmao.gsfc.nasa.gov/gmaoftp/lott/CH4/wetlands/>. Oil, gas, and coal emissions from the GFEIv2  
420 inventory are available at <https://doi.org/10.7910/DVN/HH4EUM> and other anthropogenic emissions are available from EDGARv6 at <https://doi.org/10.2760/074804>. Regional anthropogenic emissions are available for the contiguous US (<https://www.epa.gov/ghgemissions/gridded-2012-methane-emissions>), Canada (<https://doi.org/10.7910/DVN/CC3KLO>), and Mexico (<https://doi.org/10.7910/DVN/5FUTWM>). GRACE-FO data are from <https://doi.org/10.5067/TEMSC-3JC634>. Scaled OH fields, the stratospheric-adjusted GEOS-Chem restart file, stratospheric loss rates, CHEEREIO configuration files, and base HEMCO configuration file required to reproduce this work are permanently archived on Zenodo at <https://doi.org/10.5281/zenodo.15120760>. Monthly gridded posterior emissions for the posterior best estimate is also provided at <https://doi.org/10.5281/zenodo.15120760>. Additional data related to this study can be obtained on request.

## 430 Acknowledgements

This work was supported by the NASA Carbon Monitoring System. DCP was funded in part by an NSF Graduate Research Fellowship Program (GRFP) grant. This work was funded in part by an appointment

to the NASA Postdoctoral Program at the Jet Propulsion Laboratory, California Institute of Technology, administered by Oak Ridge Associated Universities under contract with NASA.

### 435 **Competing interests**

The corresponding author has declared that none of the authors has any competing interests.

### **Author contributions**

DCP and DJJ designed the study. DCP built the CHEEREIO v1.3.1 platform and performed the inversion with contributions from NB, LE, DJV, JDE, MH, TAM, EP, and HN. NB provided the TROPOMI-  
440 GOSAT product and offered guidance. DJJ, NB, LE, DJV, JDE, MH, TAM, EP, HN, and JRW discussed results and interpretation. DCP and DJJ wrote the paper with input from all authors.

### **References**

- Balabus, N., Jacob, D. J., Lorente, A., Maasackers, J. D., Parker, R. J., Boesch, H., Chen, Z., Kelp, M. M., Nesser, H., & Varon, D. J. (2023). A blended TROPOMI+GOSAT satellite data product for  
445 atmospheric methane using machine learning to correct retrieval biases. *Atmospheric Measurement Techniques*, 16(16), 3787–3807. <https://doi.org/10.5194/amt-16-3787-2023>
- Basu, S., Lan, X., Dlugokencky, E., Michel, S., Schwietzke, S., Miller, J. B., Bruhwiler, L., Oh, Y., Tans, P. P., Apadula, F., Gatti, L. V., Jordan, A., Necki, J., Sasakawa, M., Morimoto, S., Di Iorio, T.,  
450 Lee, H., Arduini, J., & Manca, G. (2022). Estimating emissions of methane consistent with atmospheric measurements of methane and  $\delta^{13}\text{C}$  of methane. *Atmospheric Chemistry and Physics*, 22(23), 15351–15377. <https://doi.org/10.5194/acp-22-15351-2022>
- Bisht, J. S. H., Patra, P. K., Takigawa, M., Sekiya, T., Kanaya, Y., Saitoh, N., & Miyazaki, K. (2023). Estimation of  $\text{CH}_4$  emission based on an advanced 4D-LETKF assimilation system. *Geoscientific Model Development*, 16(6), 1823–1838. <https://doi.org/10.5194/gmd-16-1823-2023>
- 455 Bloom, A.A., K. Bowman, M. Lee, A.J. Turner, R. Schroeder, J.R. Worden, R.J. Weidner, K.C. McDonald, and D.J. Jacob. 2017. CMS: Global 0.5-deg Wetland Methane Emissions and Uncertainty (WetCHARTs v1.0). ORNL DAAC, Oak Ridge, Tennessee, USA. <https://doi.org/10.3334/ORNLDAAC/1502>
- Borsdorff, T., Martinez-Velarte, M. C., Sneep, M., ter Linden, M. & Landgraf, J. Random Forest  
460 Classifier for Cloud Clearing of the Operational TROPOMI XCH<sub>4</sub> Product. *Remote Sensing* 16, 1208 (2024).
- Chen, Z., Jacob, D. J., Gautam, R., Omara, M., Stavins, R. N., Stowe, R. C., Nesser, H. O., Sulprizio, M. P., Lorente, A., Varon, D. J., Lu, X., Shen, L., Qu, Z., Pendergrass, D. C., & Hancock, S. (2023). Satellite quantification of methane emissions and oil/gas methane intensities from individual  
465 countries in the Middle East and North Africa: Implications for climate action. *EGU sphere*, 1–42. <https://doi.org/10.5194/egusphere-2022-1504>

- Chen, Z., Jacob, D. J., Lin, H., Balasus, N., Hardy, A., East, J., Zhang, Y., Runkle, B., Hancock, S., & Taylor, C. (2024). *Global Rice Paddy Inventory (GRPI): A high-resolution inventory of methane emissions from rice agriculture based on Landsat satellite inundation data*.  
470 <https://eartharxiv.org/repository/view/7890/>
- Crippa, M., Guizzardi, D., Solazzo, E., Muntean, M., Schaaf, E., Monforti-Ferrario, F., Banja, M., Olivier, J., Grassi, G., Rossi, S. and Vignati, E., GHG emissions of all world countries, EUR 30831 EN, Publications Office of the European Union, Luxembourg, 2021, ISBN 978-92-76-41547-3, doi:10.2760/074804, JRC126363
- 475 Cusworth, D. H., Thorpe, A. K., Ayasse, A. K., Stepp, D., Heckler, J., Asner, G. P., Miller, C. E., Yadav, V., Chapman, J. W., Eastwood, M. L., Green, R. O., Hmiel, B., Lyon, D. R., & Duren, R. M. (2022). Strong methane point sources contribute a disproportionate fraction of total emissions across multiple basins in the United States. *Proceedings of the National Academy of Sciences*, 119(38), e2202338119. <https://doi.org/10.1073/pnas.2202338119>
- 480 Drinkwater, A., Palmer, P. I., Feng, L., Arnold, T., Lan, X., Michel, S. E., Parker, R., & Boesch, H. (2023). Atmospheric data support a multi-decadal shift in the global methane budget towards natural tropical emissions. *Atmospheric Chemistry and Physics*, 23(14), 8429–8452. <https://doi.org/10.5194/acp-23-8429-2023>
- Dong, B., Peng, S., Liu, G., Pu, T., Gerlein-Safdi, C., Prigent, C., & Lin, X. (2024). Underestimation of  
485 Methane Emissions From the Sudd Wetland: Unraveling the Impact of Wetland Extent Dynamics. *Geophysical Research Letters*, 51(16), e2024GL110690. <https://doi.org/10.1029/2024GL110690>
- Duren, R. M., Thorpe, A. K., Foster, K. T., Rafiq, T., Hopkins, F. M., Yadav, V., Bue, B. D., Thompson, D. R., Conley, S., Colombi, N. K., Frankenberg, C., McCubbin, I. B., Eastwood, M. L., Falk, M., Herner, J. D., Croes, B. E., Green, R. O., & Miller, C. E. (2019). California’s methane super-emitters. *Nature*, 575(7781), Article 7781. <https://doi.org/10.1038/s41586-019-1720-3>
- 490 East, J. D., Jacob, D. J., Balasus, N., Bloom, A. A., Bruhwiler, L., Chen, Z., Kaplan, J. O., Mickley, L. J., Mooring, T. A., Penn, E., Poulter, B., Sulprizio, M. P., Worden, J. R., Yantosca, R. M., & Zhang, Z. (2024). Interpreting the Seasonality of Atmospheric Methane. *Geophysical Research Letters*, 51(10), e2024GL108494. <https://doi.org/10.1029/2024GL108494>
- 495 Eskes, H. J., Velthoven, P. F. J. V., Valks, P. J. M., & Kelder, H. M. (2003). Assimilation of GOME total-ozone satellite observations in a three-dimensional tracer-transport model. *Quarterly Journal of the Royal Meteorological Society*, 129(590), 1663–1681. <https://doi.org/10.1256/qj.02.14>
- Etioppe, G., Ciotoli, G., Schwietzke, S., & Schoell, M. (2019). Gridded maps of geological methane emissions and their isotopic signature. *Earth System Science Data*, 11(1), 1–22.  
500 <https://doi.org/10.5194/essd-11-1-2019>
- Feng, L., Palmer, P. I., Bösch, H., Parker, R. J., Webb, A. J., Correia, C. S. C., Deutscher, N. M., Domingues, L. G., Feist, D. G., Gatti, L. V., Gloor, E., Hase, F., Kivi, R., Liu, Y., Miller, J. B., Morino, I., Sussmann, R., Strong, K., Uchino, O., ... Zahn, A. (2017). Consistent regional fluxes of CH<sub>4</sub> and CO<sub>2</sub> inferred from GOSAT proxy XCH<sub>4</sub>: XCO<sub>2</sub> retrievals, 2010–2014. *Atmospheric Chemistry and Physics*, 17(7), 4781–4797. <https://doi.org/10.5194/acp-17-4781-2017>
- 505 Feng, L., Palmer, P. I., Parker, R. J., Lunt, M. F., & Bösch, H. (2023). Methane emissions are predominantly responsible for record-breaking atmospheric methane growth rates in 2020 and

2021. *Atmospheric Chemistry and Physics*, 23(8), 4863–4880. <https://doi.org/10.5194/acp-23-4863-2023>
- 510 Fung, I., John, J., Lerner, J., Matthews, E., Prather, M., Steele, L. P., & Fraser, P. J. (1991). Three-dimensional model synthesis of the global methane cycle. *Journal of Geophysical Research: Atmospheres*, 96(D7), 13033–13065. <https://doi.org/10.1029/91JD01247>
- Gaspari, G., & Cohn, S. E. (1999). Construction of correlation functions in two and three dimensions. *Quarterly Journal of the Royal Meteorological Society*, 125(554), 723–757. <https://doi.org/10.1002/qj.49712555417>
- 515 Hancock, S. E., Jacob, D. J., Chen, Z., Nesser, H., Davitt, A., Varon, D. J., Sulprizio, M. P., Balasus, N., Estrada, L. A., Cazorla, M., Dawidowski, L., Diez, S., East, J. D., Penn, E., Randles, C. A., Worden, J., Aben, I., Parker, R. J., & Maasakkers, J. D. (2025). Satellite quantification of methane emissions from South American countries: A high-resolution inversion of TROPOMI and
- 520 GOSAT observations. *Atmospheric Chemistry and Physics*, 25(2), 797–817. <https://doi.org/10.5194/acp-25-797-2025>
- Hardy, A., Palmer, P. I., & Oakes, G. (2023). Satellite data reveal how Sudd wetland dynamics are linked with globally-significant methane emissions. *Environmental Research Letters*, 18(7), 074044. <https://doi.org/10.1088/1748-9326/ace272>
- 525 Hausmann, P., Sussmann, R., & Smale, D. (2016). Contribution of oil and natural gas production to renewed increase in atmospheric methane (2007–2014): Top-down estimate from ethane and methane column observations. *Atmospheric Chemistry and Physics*, 16(5), 3227–3244. <https://doi.org/10.5194/acp-16-3227-2016>
- Houweling, S., Bergamaschi, P., Chevallier, F., Heimann, M., Kaminski, T., Krol, M., Michalak, A. M., & Patra, P. (2017). Global inverse modeling of CH<sub>4</sub> sources and sinks: An overview of methods. *Atmospheric Chemistry and Physics*, 17(1), 235–256. <https://doi.org/10.5194/acp-17-235-2017>
- 530 Hmiel, B., Petrenko, V. V., Dyonisius, M. N., Buizert, C., Smith, A. M., Place, P. F., Harth, C., Beaudette, R., Hua, Q., Yang, B., Vimont, I., Michel, S. E., Severinghaus, J. P., Etheridge, D., Bromley, T., Schmitt, J., Faïn, X., Weiss, R. F., & Dlugokencky, E. (2020). Preindustrial 14CH<sub>4</sub> indicates greater anthropogenic fossil CH<sub>4</sub> emissions. *Nature*, 578(7795), 409–412. <https://doi.org/10.1038/s41586-020-1991-8>
- 535 Hunt, B. R., Kostelich, E. J., & Szunyogh, I. (2007). Efficient data assimilation for spatiotemporal chaos: A local ensemble transform Kalman filter. *Physica D: Nonlinear Phenomena*, 230(1), 112–126. <https://doi.org/10.1016/j.physd.2006.11.008>
- 540 IPCC (2019). Refinement to the 2006 IPCC Guidelines for National Greenhouse Gas Inventories, edited by: Calvo Buendia, E., Tanabe, K., Kranjc, A., Jamsranjav, B., Fukuda, M., Ngarize, S., Osako, A., Pyrozhenko, Y., Shermanau, P., and Federici, S., IPCC, Switzerland, <https://www.ipcc.ch/report/2019-refinement-to-the-2006-ipcc-guidelines-for-national-greenhouse-gas-inventories/> (last access: 23 February 2023), 2019.
- 545 Jacob, D. J., Turner, A. J., Maasakkers, J. D., Sheng, J., Sun, K., Liu, X., Chance, K., Aben, I., McKeever, J., & Frankenberg, C. (2016). Satellite observations of atmospheric methane and their value for quantifying methane emissions. *Atmospheric Chemistry and Physics*, 16(22), 14371–14396. <https://doi.org/10.5194/acp-16-14371-2016>

- 550 Jacob, D. J., Varon, D. J., Cusworth, D. H., Dennison, P. E., Frankenberg, C., Gautam, R., Guanter, L.,  
Kelley, J., McKeever, J., Ott, L. E., Poulter, B., Qu, Z., Thorpe, A. K., Worden, J. R., & Duren,  
R. M. (2022). Quantifying methane emissions from the global scale down to point sources using  
satellite observations of atmospheric methane. *Atmospheric Chemistry and Physics*, 22(14),  
9617–9646. <https://doi.org/10.5194/acp-22-9617-2022>
- 555 Kalnay, E., & Yang, S.-C. (2010). Accelerating the spin-up of Ensemble Kalman Filtering. *Quarterly  
Journal of the Royal Meteorological Society*, 136(651), 1644–1651.  
<https://doi.org/10.1002/qj.652>
- 560 Lin, H., Jacob, D. J., Lundgren, E. W., Sulprizio, M. P., Keller, C. A., Fritz, T. M., Eastham, S. D.,  
Emmons, L. K., Campbell, P. C., Baker, B., Saylor, R. D., & Montuoro, R. (2021). Harmonized  
Emissions Component (HEMCO) 3.0 as a versatile emissions component for atmospheric models:  
Application in the GEOS-Chem, NASA GEOS, WRF-GC, CESM2, NOAA GEFS-Aerosol, and  
NOAA UFS models. *Geoscientific Model Development*, 14(9), 5487–5506.  
<https://doi.org/10.5194/gmd-14-5487-2021>
- 565 Lin, X., Peng, S., Ciais, P., Hauglustaine, D., Lan, X., Liu, G., Ramonet, M., Xi, Y., Yin, Y., Zhang, Z.,  
Bösch, H., Bousquet, P., Chevallier, F., Dong, B., Gerlein-Safdi, C., Halder, S., Parker, R. J.,  
Poulter, B., Pu, T., ... Zheng, B. (2024). Recent methane surges reveal heightened emissions from  
tropical inundated areas. *Nature Communications*, 15(1), 10894. <https://doi.org/10.1038/s41467-024-55266-y>
- 570 Liu, Y., Kalnay, E., Zeng, N., Asrar, G., Chen, Z., & Jia, B. (2019). Estimating surface carbon fluxes  
based on a local ensemble transform Kalman filter with a short assimilation window and a long  
observation window: An observing system simulation experiment test in GEOS-Chem 10.1.  
*Geoscientific Model Development*, 12(7), 2899–2914. <https://doi.org/10.5194/gmd-12-2899-2019>
- 575 Lorente, A., Borsdorff, T., Butz, A., Hasekamp, O., aan de Brugh, J., Schneider, A., Wu, L., Hase, F.,  
Kivi, R., Wunch, D., Pollard, D. F., Shiomi, K., Deutscher, N. M., Velasco, V. A., Roehl, C. M.,  
Wennberg, P. O., Warneke, T., & Landgraf, J. (2021). Methane retrieved from TROPOMI:  
Improvement of the data product and validation of the first 2 years of measurements. *Atmospheric  
Measurement Techniques*, 14(1), 665–684. <https://doi.org/10.5194/amt-14-665-2021>
- 580 Maasakkers, J. D., Jacob, D. J., Sulprizio, M. P., Turner, A. J., Weitz, M., Wirth, T., Hight, C.,  
DeFigueiredo, M., Desai, M., Schmeltz, R., Hockstad, L., Bloom, A. A., Bowman, K. W., Jeong,  
S., & Fischer, M. L. (2016). Gridded National Inventory of U.S. Methane Emissions.  
*Environmental Science & Technology*, 50(23), 13123–13133.  
<https://doi.org/10.1021/acs.est.6b02878>
- 585 Maasakkers, J. D., Jacob, D. J., Sulprizio, M. P., Scarpelli, T. R., Nesser, H., Sheng, J.-X., Zhang, Y.,  
Hersher, M., Bloom, A. A., Bowman, K. W., Worden, J. R., Janssens-Maenhout, G., & Parker, R.  
J. (2019). Global distribution of methane emissions, emission trends, and OH concentrations and  
trends inferred from an inversion of GOSAT satellite data for 2010–2015. *Atmospheric Chemistry  
and Physics*, 19(11), 7859–7881. <https://doi.org/10.5194/acp-19-7859-2019>
- 590 Miller, S. M., Michalak, A. M., & Levi, P. J. (2014). Atmospheric inverse modeling with known physical  
bounds: An example from trace gas emissions. *Geoscientific Model Development*, 7(1), 303–315.  
<https://doi.org/10.5194/gmd-7-303-2014>

- Miyazaki, K., Eskes, H. J., & Sudo, K. (2012). Global NO<sub>x</sub> emission estimates derived from an assimilation of OMI tropospheric NO<sub>2</sub> columns. *Atmospheric Chemistry and Physics*, 12(5), 2263–2288. <https://doi.org/10.5194/acp-12-2263-2012>
- 595 Mooring, T. A., Jacob, D. J., Sulprizio, M. P., Balasus, N., Baier, B. C., Kiefer, M., et al. (2024). Evaluating Stratospheric Methane in GEOS-Chem with Satellite and Balloon Observations. Presented at the American Meteorological Society 104th Annual Meeting, Baltimore, MD, USA. Retrieved from <https://ams.confex.com/ams/104ANNUAL/meetingapp.cgi/Paper/437083>
- 600 Murguia-Flores, F., Arndt, S., Ganesan, A. L., Murray-Tortarolo, G., & Hornibrook, E. R. C. (2018). Soil Methanotrophy Model (MeMo v1.0): A process-based model to quantify global uptake of atmospheric methane by soil. *Geoscientific Model Development*, 11(6), 2009–2032. <https://doi.org/10.5194/gmd-11-2009-2018>
- 605 Naik, V., Szopa, S., Adhikary, B., Artaxo, P., Bernsten, T., Collins, W. D., Fuzzi, S., Gallardo, L., Kiendler Scharr, A., Klimont, Z., Liao, H., Unger, N., and Zanis, P.: Short-Lived Climate Forcers, in: *Climate Change 2021: The Physical Science Basis. Contribution of Working Group I to the Sixth Assessment Report of the Intergovernmental Panel on Climate Change*, edited by: Masson-Delmotte, V., Zhai, P., Pirani, A., Connors, S. L., Péan, C., Berger, S., Caud, N., Chen, Y., Goldfarb, L., Gomis, M. L., Huang, M., Leitzell, K., Lonnoy, E., Matthews, J. B. R., Maycock, T. K., Waterfield, T., Yelekçi, O., Yu, R., and Zhou, B., Cambridge University Press, [https://www.ipcc.ch/report/ar6/wg1/downloads/report/IPCC\\_AR6\\_WGI\\_Chapter06.pdf](https://www.ipcc.ch/report/ar6/wg1/downloads/report/IPCC_AR6_WGI_Chapter06.pdf) (last access: 21 Feb 2023), 2021
- 610 Nisbet, E. G., Fisher, R. E., Lowry, D., France, J. L., Allen, G., Bakkaloglu, S., Broderick, T. J., Cain, M., Coleman, M., Fernandez, J., Forster, G., Griffiths, P. T., Iverach, C. P., Kelly, B. F. J., Manning, M. R., Nisbet-Jones, P. B. R., Pyle, J. A., Townsend-Small, A., al-Shalaan, A., ... Zazzeri, G. (2020). Methane Mitigation: Methods to Reduce Emissions, on the Path to the Paris Agreement. *Reviews of Geophysics*, 58(1), e2019RG000675. <https://doi.org/10.1029/2019RG000675>
- NOAA (2024). Global CH<sub>4</sub> Monthly Means, available at: [https://gml.noaa.gov/ccgg/trends\\_ch4/](https://gml.noaa.gov/ccgg/trends_ch4/)
- 620 Pandey, S., Houweling, S., Lorente, A., Borsdorff, T., Tsvilidou, M., Bloom, A. A., Poulter, B., Zhang, Z., & Aben, I. (2021). Using satellite data to identify the methane emission controls of South Sudan's wetlands. *Biogeosciences*, 18(2), 557–572. <https://doi.org/10.5194/bg-18-557-2021>
- Pendergrass, D. C., Jacob, D. J., Nesser, H., Varon, D. J., Sulprizio, M., Miyazaki, K., & Bowman, K. W. (2023). CHEEREIO 1.0: A versatile and user-friendly ensemble-based chemical data assimilation and emissions inversion platform for the GEOS-Chem chemical transport model. *Geoscientific Model Development*, 16(16), 4793–4810. <https://doi.org/10.5194/gmd-16-4793-2023>.
- 625 Peng, S., Lin, X., Thompson, R. L., Xi, Y., Liu, G., Hauglustaine, D., Lan, X., Poulter, B., Ramonet, M., Saunio, M., Yin, Y., Zhang, Z., Zheng, B., & Ciais, P. (2022). Wetland emission and atmospheric sink changes explain methane growth in 2020. *Nature*, 612(7940), 477–482. <https://doi.org/10.1038/s41586-022-05447-w>
- 630 Penn, E., Jacob, D. J., Chen, Z., East, J. D., Sulprizio, M. P., Bruhwiler, L., Maasackers, J. D., Nesser, H., Qu, Z., Zhang, Y., & Worden, J. (2025). What can we learn about tropospheric OH from satellite observations of methane? *Atmospheric Chemistry and Physics*, 25(5), 2947–2965. <https://doi.org/10.5194/acp-25-2947-2025>

- Prather, M. J., Holmes, C. D., & Hsu, J. (2012). Reactive greenhouse gas scenarios: Systematic exploration of uncertainties and the role of atmospheric chemistry. *Geophysical Research Letters*, 39(9). <https://doi.org/10.1029/2012GL051440>
- 635 Qu, Z., Jacob, D. J., Shen, L., Lu, X., Zhang, Y., Scarpelli, T. R., Nesser, H., Sulprizio, M. P., Maasakkers, J. D., Bloom, A. A., Worden, J. R., Parker, R. J., & Delgado, A. L. (2021). Global distribution of methane emissions: A comparative inverse analysis of observations from the TROPOMI and GOSAT satellite instruments. *Atmospheric Chemistry and Physics*, 21(18), 14159–14175. <https://doi.org/10.5194/acp-21-14159-2021>
- 640 Qu, Z., Jacob, D. J., Zhang, Y., Shen, L., Varon, D. J., Lu, X., Scarpelli, T., Bloom, A., Worden, J., & Parker, R. J. (2022). Attribution of the 2020 surge in atmospheric methane by inverse analysis of GOSAT observations. *Environmental Research Letters*, 17(9), 094003. <https://doi.org/10.1088/1748-9326/ac8754>
- 645 Qu, Z., Jacob, D. J., Bloom, A. A., Worden, J. R., Parker, R. J., & Boesch, H. (2024). Inverse modeling of 2010–2022 satellite observations shows that inundation of the wet tropics drove the 2020–2022 methane surge. *Proceedings of the National Academy of Sciences*, 121(40), e2402730121. <https://doi.org/10.1073/pnas.2402730121>
- 650 Sabbatino, M., Romeo, L., Baker, V., Bauer, J., Barkhurst, A., Bean, A., DiGiulio, J., Jones, K., Jones, T.J., Justman, D., Miller III, R., Rose, K., and Tong., A., Global Oil & Gas Features Database, 2017-12-12, <https://edx.netl.doe.gov/dataset/global-oil-gas-features-database> , DOI: 10.18141/1427300
- Saunio, M., Martinez, A., Poulter, B., Zhang, Z., Raymond, P., Regnier, P., Canadell, J. G., Jackson, R. B., Patra, P. K., Bousquet, P., Ciais, P., Dlugokencky, E. J., Lan, X., Allen, G. H., Bastviken, D., Beerling, D. J., Belikov, D. A., Blake, D. R., Castaldi, S., ... Zhuang, Q. (2024). Global Methane Budget 2000–2020. *Earth System Science Data Discussions*, 1–147. <https://doi.org/10.5194/essd-2024-115>
- 655 Scarpelli, T. R., Jacob, D. J., Villasana, C. A. O., Hernández, I. F. R., Moreno, P. R. C., Alfaro, E. A. C., García, M. Á. G., & Zavala-Araiza, D. (2020). A gridded inventory of anthropogenic methane emissions from Mexico based on Mexico’s national inventory of greenhouse gases and compounds. *Environmental Research Letters*, 15(10), 105015. <https://doi.org/10.1088/1748-9326/abb42b>
- 660 Scarpelli, T. R., Jacob, D. J., Moran, M., Reuland, F., & Gordon, D. (2021). A gridded inventory of Canada’s anthropogenic methane emissions. *Environmental Research Letters*, 17(1), 014007. <https://doi.org/10.1088/1748-9326/ac40b1>
- 665 Scarpelli, T. R., Jacob, D. J., Grossman, S., Lu, X., Qu, Z., Sulprizio, M. P., Zhang, Y., Reuland, F., Gordon, D., & Worden, J. R. (2022). Updated Global Fuel Exploitation Inventory (GFEI) for methane emissions from the oil, gas, and coal sectors: Evaluation with inversions of atmospheric methane observations. *Atmospheric Chemistry and Physics*, 22(5), 3235–3249. <https://doi.org/10.5194/acp-22-3235-2022>
- 670 van der Werf, G. R., Randerson, J. T., Giglio, L., van Leeuwen, T. T., Chen, Y., Rogers, B. M., Mu, M., van Marle, M. J. E., Morton, D. C., Collatz, G. J., Yokelson, R. J., & Kasibhatla, P. S. (2017). Global fire emissions estimates during 1997–2016. *Earth System Science Data*, 9(2), 697–720. <https://doi.org/10.5194/essd-9-697-2017>

- 675 Vanselow, S., Schneising, O., Buchwitz, M., Reuter, M., Bovensmann, H., Boesch, H., & Burrows, J. P. (2024). Automated detection of regions with persistently enhanced methane concentrations using Sentinel-5 Precursor satellite data. *Atmospheric Chemistry and Physics*, 24(18), 10441–10473. <https://doi.org/10.5194/acp-24-10441-2024>
- Varon, D. J., et al. In prep.
- 680 Wang, X., Jacob, D. J., Eastham, S. D., Sulprizio, M. P., Zhu, L., Chen, Q., Alexander, B., Sherwen, T., Evans, M. J., Lee, B. H., Haskins, J. D., Lopez-Hilfiker, F. D., Thornton, J. A., Huey, G. L., & Liao, H. (2019). The role of chlorine in global tropospheric chemistry. *Atmospheric Chemistry and Physics*, 19(6), 3981–4003. <https://doi.org/10.5194/acp-19-3981-2019>
- 685 Watkins, M. M., Wiese, D. N., Yuan, D.-N., Boening, C., & Landerer, F. W. (2015). Improved methods for observing Earth’s time variable mass distribution with GRACE using spherical cap mascons. *Journal of Geophysical Research: Solid Earth*, 120(4), 2648–2671. <https://doi.org/10.1002/2014JB011547>
- Wecht, K. J., Jacob, D. J., Frankenberg, C., Jiang, Z., & Blake, D. R. (2014). Mapping of North American methane emissions with high spatial resolution by inversion of SCIAMACHY satellite data. *Journal of Geophysical Research: Atmospheres*, 119(12), 7741–7756. <https://doi.org/10.1002/2014JD021551>
- 690 West, J. J., Fiore, A. M., Horowitz, L. W., & Mauzerall, D. L. (2006). Global health benefits of mitigating ozone pollution with methane emission controls. *Proceedings of the National Academy of Sciences*, 103(11), 3988–3993. <https://doi.org/10.1073/pnas.0600201103>
- 695 Whitaker, J. S., & Hamill, T. M. (2012). Evaluating Methods to Account for System Errors in Ensemble Data Assimilation. *Monthly Weather Review*, 140(9), 3078–3089. <https://doi.org/10.1175/MWR-D-11-00276.1>
- 700 Wiese, D. N., Landerer, F. W., & Watkins, M. M. (2016). Quantifying and reducing leakage errors in the JPL RL05M GRACE mascon solution. *Water Resources Research*, 52(9), 7490–7502. <https://doi.org/10.1002/2016WR019344>
- Wiese, D. N., D.-N. Yuan, C. Boening, F. W. Landerer, M. M. Watkins. 2023. JPL GRACE and GRACE-FO Mascon Ocean, Ice, and Hydrology Equivalent Water Height CRI Filtered RL06.3Mv04. Ver. RL06.3Mv04. PO.DAAC, CA, USA. Dataset accessed [2025-02-07] at <https://doi.org/10.5067/TEMSC-3JC634>
- 705 Yu, X., Millet, D. B., & Henze, D. K. (2021). How well can inverse analyses of high-resolution satellite data resolve heterogeneous methane fluxes? Observing system simulation experiments with the GEOS-Chem adjoint model (v35). *Geoscientific Model Development*, 14(12), 7775–7793. <https://doi.org/10.5194/gmd-14-7775-2021>
- 710 Yu, X., Millet, D. B., Henze, D. K., Turner, A. J., Delgado, A. L., Bloom, A. A., & Sheng, J. (2023). A high-resolution satellite-based map of global methane emissions reveals missing wetland, fossil fuel, and monsoon sources. *Atmospheric Chemistry and Physics*, 23(5), 3325–3346. <https://doi.org/10.5194/acp-23-3325-2023>
- Zhang, B., Tian, H., Ren, W., Tao, B., Lu, C., Yang, J., Banger, K., & Pan, S. (2016a). Methane emissions from global rice fields: Magnitude, spatiotemporal patterns, and environmental controls. *Global Biogeochemical Cycles*, 30(9), 1246–1263. <https://doi.org/10.1002/2016GB005381>
- 715

- Zhang, Z., Zimmermann, N. E., Kaplan, J. O., & Poulter, B. (2016b). Modeling spatiotemporal dynamics of global wetlands: Comprehensive evaluation of a new sub-grid TOPMODEL parameterization and uncertainties. *Biogeosciences*, 13(5), 1387–1408. <https://doi.org/10.5194/bg-13-1387-2016>
- 720 Zhang, Y., Jacob, D. J., Lu, X., Maasakkers, J. D., Scarpelli, T. R., Sheng, J.-X., Shen, L., Qu, Z., Sulprizio, M. P., Chang, J., Bloom, A. A., Ma, S., Worden, J., Parker, R. J., & Boesch, H. (2021). Attribution of the accelerating increase in atmospheric methane during 2010–2018 by inverse analysis of GOSAT observations. *Atmospheric Chemistry and Physics*, 21(5), 3643–3666. <https://doi.org/10.5194/acp-21-3643-2021>
- 725 Zhu, S., Feng, L., Liu, Y., Wang, J., & Yang, D. (2022). Decadal Methane Emission Trend Inferred from Proxy GOSAT XCH<sub>4</sub> Retrievals: Impacts of Transport Model Spatial Resolution. *Advances in Atmospheric Sciences*, 39(8), 1343–1359. <https://doi.org/10.1007/s00376-022-1434-6>